JGR Earth Surface

RESEARCH ARTICLE
10.1029/2021JF006520

The Significance of Convection in Supraglacial Debris Revealed Through Novel Analysis of Thermistor Profiles

Eric Petersen[1], Regine Hock[1,2], Gilberto J. Fochesatto[3], and Leif S. Anderson[4]

[1]Geophysical Institute, University of Alaska Fairbanks, Fairbanks, AK, USA, [2]Department of Geosciences, University of Oslo, Oslo, Norway, [3]Department of Atmospheric Sciences, University of Alaska Fairbanks, Fairbanks, AK, USA, [4]Department of Geology and Geophysics, University of Utah, Salt Lake City, UT, USA

Key Points:

- We developed a new method to constrain supraglacial debris thermal properties and nonconductive heat fluxes from temperature profile data
- Nonconductive heat flux can be as much as 43% the conductive heat flux, thus it is important to understand its driving processes
- We interpret nonconductive heat flux to be dominated by convection of moisture and latent heat flux as the debris diurnally wets and dries

Correspondence to:
E. Petersen,
eipetersen@alaska.edu

Citation:
Petersen, E., Hock, R., Fochesatto, G. J., & Anderson, L. S. (2022). The significance of convection in supraglacial debris revealed through novel analysis of thermistor profiles. *Journal of Geophysical Research: Earth Surface*, *127*, e2021JF006520. https://doi.org/10.1029/2021JF006520

Received 16 NOV 2021
Accepted 23 AUG 2022

Author Contributions:
Conceptualization: Eric Petersen
Data curation: Eric Petersen, Leif S. Anderson
Formal analysis: Eric Petersen
Funding acquisition: Regine Hock
Investigation: Eric Petersen, Gilberto J. Fochesatto
Methodology: Eric Petersen
Project Administration: Eric Petersen, Regine Hock
Resources: Regine Hock, Gilberto J. Fochesatto, Leif S. Anderson
Supervision: Eric Petersen, Regine Hock
Visualization: Eric Petersen
Writing – original draft: Eric Petersen
Writing – review & editing: Eric Petersen, Regine Hock, Gilberto J. Fochesatto, Leif S. Anderson

Abstract Melt from debris-covered glaciers represents a regionally important freshwater source, especially in high-relief settings as found in central Asia, Alaska, and South America. Sub-debris melt is traditionally predicted from surface energy balance models that determine heat conduction through the supraglacial debris layer. Convection is rarely addressed, despite the porous nature of debris. Here we provide the first constraints on convection in supraglacial debris, through the development of a novel method to calculate individual conductive and nonconductive heat flux components from debris temperature profile data. This method was applied to data from Kennicott Glacier, Alaska, spanning two weeks in the summer of 2011 and two months in the summer of 2020. Both heat flux components exhibit diurnal cycles, the amplitude of which is coupled to atmospheric conditions. Mean diurnal nonconductive heat flux peaks at up to 43% the value of conductive heat flux, indicating that failure to account for it may lead to an incorrect representation of melt rates and their drivers. We interpret this heat flux to be dominated by latent heat as debris moisture content changes on a diurnal cycle. A sharp afternoon drop-off in nonconductive heat flux is observed at shallow depths as debris dries. We expect these processes to be relevant for other debris-covered glaciers. Debris properties such as porosity and tortuosity may play a large role in modulating it. Based on the present analysis, we recommend further study of convection in supraglacial debris for glaciers across the globe with different debris properties.

Plain Language Summary Glacier melt under a surface layer of rocky debris is typically predicted by determining the energy available at the debris surface, then calculating heat transferred via conduction through the debris layer. However, heat can also be transferred in the debris layer through other processes such as air movement and the evaporation of melt water. We analyzed temperature data in the debris to show that these processes are significant, accounting for up to 43% of heat transferred via conduction. These must thus be investigated further and incorporated into models of glacier melt.

1. Introduction

Supraglacial debris cover is widespread on glaciers in Alaska and High Mountain Asia, where it covers 9%–14% and 10%–19% of total glacier surface area, respectively (D. Scherler et al., 2018; Herreid & Pellicciotti, 2018). For these regions it has a strong effect on regional melt rates (e.g., Bhushan et al. (2018)), with implications for regional freshwater resources and hydrology. Debris-covered area is also widely expected to expand as glaciers retreat and thin worldwide in response to climate change (e.g., Thakuri et al., 2014). Understanding the effect of supraglacial debris on melt rates worldwide is therefore critical to effectively predict glacier melt and subsequent effects on hydrology into the future.

Supraglacial debris is generally sourced from weathering of the glacier's headwalls and valley walls as well as bed erosion and is largely composed of unsorted angular clasts from sand and silt-sized up to large boulders (Boulton, 1978; Reheis, 1975; van Woerkom et al., 2019). Debris is a powerful moderator of glacier melt, with the relationship between sub-debris melt rates and debris thickness being empirically described by the Østrem curve (Østrem, 1959). For thin debris cover melt is increased relative to a bare ice surface, but for a sufficiently thick debris layer (typically on the order of a few centimeters for rocky debris) sub-debris melt rates become attenuated (Bozhinskiy et al., 1986; Dolgushin, 1972; Khodakov, 1972; Mattson et al., 1993; Østrem, 1959). The behavior of the Østrem curve comes from the debris cover's effect on the surface energy balance. Surface debris typically has an albedo of 0.1–0.4 (Inoue & Yoshida, 1980; Kayastha et al., 2000; Lejeune et al., 2013; Nicholson & Benn, 2012; Rounce et al., 2018), compared to glacier ice albedo of 0.30–0.46 (Cuffey & Paterson, 2010); thus,

debris is more effective at absorbing shortwave solar radiation. Because thickened supraglacial debris typically leads to higher debris surface temperatures than ice surface or air temperatures (Conway & Rasmussen, 2000; Reid et al., 2012; Rowan et al., 2020), it also more effectively cools itself via emission of longwave radiation and through sensible and latent heat fluxes (e.g., Nicholson and Stiperski (2020); Steiner et al. (2018)). Longwave radiation emission and sensible heat flux were shown by Hénot et al. (2021) to be major drivers in the formation of "glacier tables," boulders on the glacier surface that rest on an ice/snow pedestal due to differential ablation.

Energy balance modeling of sub-debris melt involves evaluation of individual energy balance terms at the debris surface, imposing energy closure to constrain ground heat flux into the debris. The debris layer is then typically treated as a horizontally homogeneous medium (some vertical structure may be invoked) to calculate the conductive heat flux available for sub-debris melt, as pioneered by Reid and Brock (2010) and used further by Rounce and McKinney (2014), Nicholson and Benn (2012), Rounce et al. (2015, 2021), and Reid et al. (2012). While this approach has proven useful in many studies, it ignores convective processes which may occur within the surface debris layer, and thus heat transfer by conduction may be overestimated.

Heat convection and advection through air flow in debris has been explored in the context of rock glaciers and periglacial terrains. A well-known mechanism is that of the "chimney effect," whereby an ascending circulation of winter air through sloped porous sediments efficiently cools the subsurface (Delaloye & Lambiel, 2005; Morard et al., 2010). Convection in talus has been modeled by Wicky and Hauck (2020), who found that high debris permeability and thermal gradient leads to convection playing a crucial role. M. Scherler et al. (2014) produced a more complex model, highlighting the importance of thermal radiation between debris blocks, turbulent heat fluxes, and freeze/thaw cycling.

Convection can be significant in other contexts, such as within subarctic snowpack (Sturm & Benson, 1997; Sturm & Johnson, 1991) and in the permafrost active layer (Roth & Boike, 2001), which suggests they may be significant for debris-covered glaciers as well. Nicholson and Benn (2012) identified nonlinear behavior in mean temperature profiles for coarse supraglacial debris cover on the Ngozumpa Glacier, which they interpreted as evidence for convection cooling the uppermost debris layer.

Debris moisture content may vary dramatically on the seasonal, diurnal, and hourly timescale in response to sub-debris melt rates, supraglacial hydrology, precipitation, and drying. This in turn could lead to changes in debris layer thermal conductivity (Nicholson & Benn, 2006) as well as latent heat fluxes as the debris layer periodically wets and dries. This poor understanding of debris layer wetting and drying also means that latent heat fluxes on debris-covered glaciers (surface and subsurface) may be poorly represented in physical models. Most models assume a debris layer with a totally dry or saturated state, either consistently for the entire model period (Lejeune et al., 2013; Nicholson & Benn, 2006), or exhibiting periods of saturation defined by measured surface relative humidity of 100% (Reid & Brock, 2010) or precipitation events (Rounce et al., 2015). In some cases, however, modeling efforts have investigated these processes in greater detail. Collier et al. (2014) developed an energy balance model including a reservoir module in which the porous debris layer fills with melt water to aid in the calculation of latent heat fluxes. The latent heat flux is then calculated at the surface, separating saturated debris from dry debris. Evatt et al. (2015) developed idealized analytical solutions to model how the infiltration of air into a porous debris layer produces sensible heat fluxes within the debris as well as latent heat fluxes evaluated at the ice surface. Their model was successful at reproducing the shape of the Østrem curve for low debris thicknesses, with melt rates rising from 0 cm debris to maximum melt rates at 1–2 cm debris and melt suppression at >4 cm debris. Most models do not capture this behavior but rather produce maximum melt rates for an infinitesimally thin debris layer. Giese et al. (2020) also recently adapted a soil model incorporating vertical moisture transport to debris-covered glaciers for evaluation of latent heat fluxes at the debris surface.

Despite these recent advances in modeling, very few analyses of in situ data on debris-covered glaciers have produced constraints on water content and latent heat fluxes within or associated with the surface debris layer. Such work is necessary to constrain current models and inform the development of new, updated debris-covered glacier energy balance models.

As an added complication, surface debris thickness is highly spatially heterogeneous on debris-covered glaciers (e.g., Mihalcea et al. (2008); Nicholson et al. (2018)). This leads to melt hotspots and areas of reduced melt, which in turn produces a rough hummocky surface (Bartlett et al., 2020; Mölg et al., 2020) that feeds back on debris thickness patterns as well as atmospheric surface layer dynamics and turbulent heat transfer (Bonekamp

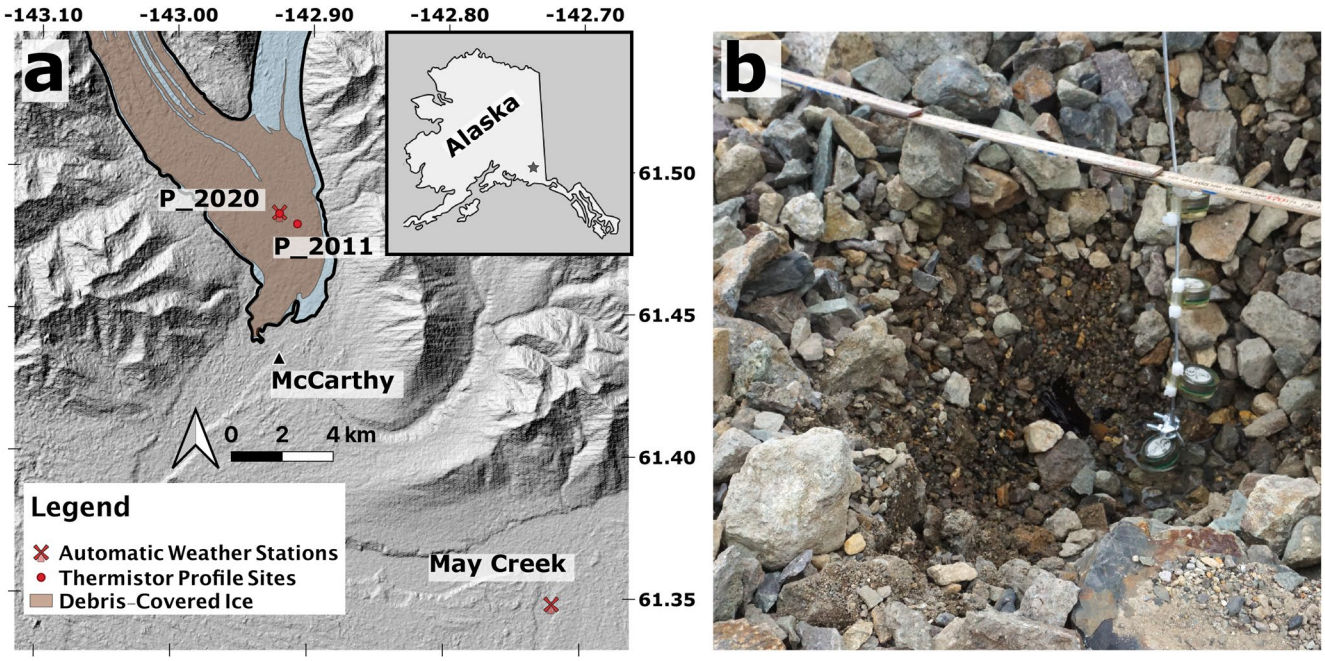

Figure 1. (a) Map of the study location, with the glacier outline from the Randolph Glacier Inventory version 6.0 shown (RGI Consortium, 2017), along with the village of McCarthy, automatic weather stations, and debris temperature profiles (two from 2020 at site "P_2020" and one from 2011 at site "P_2011") used in this study. Inset: location of study site in the state of Alaska. (b) Image of debris temperature profile (P_2020a, Table 1) being installed on 17 June 2020 with 7 cm spacing between sensors. Note the sorting of smaller pebble and sand-sized clasts toward the base of the debris layer, as well as the darker wet debris at depth exposed in the excavation.

et al., 2020; Nicholson & Stiperski, 2020; Steiner et al., 2018). As a result, the surface energy balance and debris layer heat flux may be highly spatially variable, leading to challenges in the traditional method of using surface energy balance closure to estimate ground heat flux. Thus, there is a need for more direct assessment of heat flux in surface debris.

The purpose of this study is to assess the importance of nonconductive processes within supraglacial debris, such as convection and latent heat flux, in the context of sub-debris melt. We present a novel data analysis approach for constraining the separated conductive and nonconductive heat fluxes from in situ debris temperature data on Kennicott Glacier, Alaska, collected in summer 2020 and 2011.

2. Study Site

Kennicott Glacier is a large compound valley glacier located in the Wrangell-St. Elias National Park, Alaska (Figure 1). Covering an area of 387 km^2, it descends 43 km from its accumulation areas on the southern flank of Mount Blackburn at 4,996 m a.s.l. down to its terminus at 400 m a.s.l. Abundant medial moraines coalesce to form a continuous supraglacial debris layer ~7 km from the terminus; roughly 20% of the glacier's surface area is debris-covered as of 2015 (Anderson, Armstrong, Anderson, & Buri, 2021).

Kennicott Glacier was stabilized at its modern maximum extent between 1860 and 1909 and has been steadily retreating and thinning since that time, with a mean retreat rate of roughly 7 m yr^{-1} between 1909 and 1995 (Rickman & Rosenkrans, 1997). (Das et al., 2014) found specific mass balances of −0.17 m w.e. yr^{-1} for 1957–2000 and −0.46 m w.e. yr^{-1} for 2000–2007, indicating an accelerated rate of mass loss. A study of distributed melt estimates, derived from modeling sub-debris ice, bare ice, and ice cliff melt rates for the 2011 ablation season, found area-averaged sub-debris melt rates of 1.6–4.2 cm d^{-1} over the debris-covered tongue (an area of 24 km^2 extending up to 8 km from the terminus) (Anderson, Armstrong, Anderson, & Buri, 2021). This study also found that although ice cliffs contribute disproportionately to ice melt during the ablation season (accounting for 26% of melt during the ablation season while covering only 12% of the area), the majority of melt (74%) still occurs beneath debris. Anderson, Armstrong, Anderson, Scherler, and Petersen (2021) found that the zone of

Table 1
Characteristics of Debris Temperature Profiles (Figure 1)

Profile	Period	Debris depth (cm)	t_s (min)	N	h (cm)	Debris grain size	Elev. (m a.s.l.)
P_2020a	27 July to 6 September 2020	25	5	4	7	Cobbles/pebbles over sandy cobbles/pebbles	481
P_2020b	27 July to 6 September 2020	22	5	2	10	Cobbles/pebbles over sandy cobbles/pebbles	481
P_2011	8 August to 17 August 2011	15	30	4	5	N/A	580

Note. t_s is the sampling frequency, N refers to the number of sensors in the profile and h is the mean vertical spacing of the sensors

continuous debris cover has expanded up the glacier through time, while debris thickness has thickened near the terminus as the glacier itself thinned. The rapid reduction of ice emergence rate under the debris cover accounts for most of the mass loss near the glacier terminus.

The debris cover on Kennicott Glacier is composed of a variety of rock types, including metamorphosed basalt and andesite, as well as marine limestones and sedimentary deposits (MacKevett, 1978). Its thickness has been measured at up to >40 cm, with mean debris thickness dependent on elevation ranging from 7 cm at 600 m elevation to 22 cm at 450 m elevation circa 2011 (Anderson, Armstrong, Anderson, & Buri, 2021).

3. Data

3.1. Debris Layer Temperatures

We measured in situ debris temperature throughout the summer of 2020 using temperature sensors deployed in two 22–25 cm deep vertical profiles <5 m apart from each other and located <10 m each from an on-glacier automatic weather station (AWS) (Figure 1a, Section 3.2). These profiles we refer to as "P_2020a" (4 sensors, 25 cm debris) and "P_2020b" (2 sensors, 22 cm debris).

For each location, the surface debris was removed down to the ice surface, a reference meter stick was placed across the rim of the excavation, and debris thickness was measured as the distance from the ice surface to that reference stick. We estimate the uncertainty in this debris thickness measurement to be ±1 cm. When removing the debris, care was taken to preserve the stratigraphy as best as possible. A tarp was used to store the debris and keep debris from the upper, middle, and lower sections of the layer separate; the general clast size and degree of sorting were also qualitatively described. After installation of the thermistor profiles, this debris was then replaced in the original order. It is of course impossible to replace the debris perfectly as it was found, and the thermal properties/moisture content of the debris are likely somewhat altered during the disinterment and installation process. Thus, we disregarded at least the first several days of data to allow the debris layer to re-equilibrate.

Each profile recorded data every 5 minutes and was constructed using Onset Hobo Tidbit v2 temperature sensors with built-in data loggers and a stated accuracy of ±0.2°C and resolution of ±0.02°C. The sensors were attached to a wire at prescribed spacing appropriate to the specific locations (7 and 10 cm). The uppermost sensor was covered by several centimeters of a single moderate-sized clast or a thin layer of gravel, in order to best measure near-surface temperature without being biased by direct solar radiation. An example of temperature profile installation in the debris is shown in Figure 1b.

To investigate the variability of surface debris layer heat fluxes in time and space, we also included a debris-temperature profile from 2011, located ~800 m from the 2020 sites (Figure 1), that was presented in Anderson, Armstrong, Anderson, and Buri (2021). In situ debris temperatures were measured for 8 days (8–16 August) using a chain of four iButton thermistors, which have a stated accuracy of ±1°C. This profile, which we refer to as "P_2011," was installed in 15 cm debris with variable sensor spacing between 3 and 6 cm. This profile was chosen for analysis since it was located in moraine material, which is similar to that in which the 2020 temperature profiles were planted within. Further details are given in Table 1.

3.2. Automatic Weather Stations

During summer 2020, we operated an energy balance weather station over the debris-covered portion of Kennicott Glacier (61.4842°N and 142.9238°W; 580 m a.s.l.). The station ran between 10 June and 21 August, and included

measurements of air temperature, humidity, wind speed and direction, shortwave incoming and reflected, and longwave upwelling and downwelling radiation recorded to a Campbell Scientific CR5000 data logger. In this study, we used the shortwave downwelling radiation data to support the interpretation of the results of the debris layer thermal analysis. The radiative fluxes were measured with a Hukseflux NR01 net radiometer.

For the data analysis in 2011 we used radiation data from the May Creek AWS operated by MesoWest (University of Utah), located roughly 16 km to the southeast of Kennicott Glacier's terminus (61.3475°N and 142.7205717°W; 481 m a.s.l.). The locations of both AWS are mapped in Figure 1.

3.3. Ablation Stake Data

On 17 June 2020, we drilled three ablation stakes into sub-debris ice at site P_2020 within <20 m of both the temperature profiles and the AWS. These stakes were installed under 6, 18, and 21 cm debris depth. The length of the exposed stakes was measured on 25 July and 9 September to derive surface lowering and thus total sub-debris melt over this period. Because the debris thickness for one of the ablation stakes is within error (21 ± 1 cm) of the debris thickness for temperature profile P_2020b (22 cm), we used the melt measured at that stake to compare with the temperature profile data and its associated analysis products.

4. Methods

4.1. Thermal Analysis of Debris Layer

Our analysis of debris temperatures starts with the one-dimensional heat conservation equation for the surface debris layer, which is taken as:

$$\rho c \frac{\partial T}{\partial t} = \frac{\partial}{\partial z}\left(Q_{total}\right) = \frac{\partial}{\partial z}\left(Q_c + Q_{nc}\right) = \frac{\partial}{\partial z}\left(k\frac{\partial T}{\partial z}\right) + \frac{\partial Q_{nc}}{\partial z}, \tag{1}$$

where ρ is the bulk density (in kg m^{-3}) of the debris layer (typically $\rho = \phi\rho_{\text{rock}}$, where ϕ is debris layer porosity, and ρ_{rock} the density of the rock making up the debris), c is its specific heat capacity (in J kg^{-1} K^{-1}), T is debris temperature (K), t is time (in s), z is vertical position in the debris layer (in m), and Q_{total} the sum of heat fluxes through the plane normal to the z direction (all heat fluxes in units of W/m^2). We then split the sub-debris heat flux Q_{total} into the conductive heat flux $Q_c = k_e[\partial T/\partial z]$ and the sum of residual nonconductive heat fluxes Q_{nc}. In the conductive heat flux term, k is the thermal conductivity of the debris layer. Q_{nc} includes radiation penetrating the surface and latent heat fluxes due to vapor transport and evaporation occurring within the debris layer. Considering $\frac{\partial k}{\partial z}$ to be non-negligible, we simplify the equation to the following:

$$\frac{\partial T}{\partial t} = \frac{\partial \kappa}{\partial z}\frac{\partial T}{\partial z} + \kappa\frac{\partial^2 T}{\partial z^2} + \left(\frac{1}{\rho c}\right)\frac{\partial Q_{nc}}{\partial z}, \tag{2}$$

where $\kappa = k/(\rho c)$ is termed the thermal diffusivity (units of m^2 s^{-1}). If the debris layer is assumed to be purely conductive, with $\frac{\partial Q_{nc}}{\partial z} = 0$, the relationship between the differentials $\frac{\partial T}{\partial t}$, $\frac{\partial T}{\partial z}$, and $\frac{\partial^2 T}{\partial z^2}$ can be used to constrain the thermal structure of the debris layer through κ and $\frac{\partial \kappa}{\partial z}$. We thus constrain κ and $\frac{\partial \kappa}{\partial z}$ for each debris temperature profile by performing a multiple linear regression on $\frac{\partial T}{\partial t}$ as a function of $\frac{\partial T}{\partial z}$ and $\frac{\partial^2 T}{\partial z^2}$. This method is novel in that previous work has considered $\frac{\partial \kappa}{\partial z}$ as negligible, fitting $\frac{\partial T}{\partial t}$ as a function of $\frac{\partial^2 T}{\partial z^2}$ only to constrain κ (Nicholson & Benn, 2012).

For a debris layer with nonconductive processes at play, $\frac{\partial Q_{nc}}{\partial z}$ is nonzero and expected to be variable in time, leading to altered values of $\frac{\partial T}{\partial t}$ relative to those predicted by $\frac{\partial T}{\partial z}$ and $\frac{\partial^2 T}{\partial z^2}$. We use this concept to separate Q_c from Q_{nc} in the following way. First, $\left[\frac{\partial T}{\partial t}\right]_{model}$ is predicted from measured $\frac{\partial T}{\partial z}$ and $\frac{\partial^2 T}{\partial z^2}$ and our constrained values for κ and $\frac{\partial \kappa}{\partial z}$. Then, the residual between $\left[\frac{\partial T}{\partial t}\right]_{obs}$ calculated from observations and $\left[\frac{\partial T}{\partial t}\right]_{model}$ predicted from the model is used to estimate $\frac{\partial Q_{nc}}{\partial z}$:

$$\frac{\partial Q_{nc}}{\partial z} = \rho c\left(\left[\frac{\partial T}{\partial t}\right]_{obs} - \left[\frac{\partial T}{\partial t}\right]_{model}\right). \tag{3}$$

$\frac{\partial Q_{nc}}{\partial z}$ is reported in this work in units of W m^{-2} cm^{-1}, as this treatment returns the change in heat flux in W m^{-2} for each vertical cm in the surface debris layer. The determined value of $\frac{\partial Q_{nc}}{\partial z}$ can then be integrated along z to estimate the value of Q_{nc} at different levels in the debris layer:

$$Q_{nc} = \int \frac{\partial Q_{nc}}{\partial z} dz \tag{4}$$

4.2. Boundary Conditions

To solve explicitly for Q_{nc}, appropriate boundary conditions must be introduced. For this work, we apply the boundary condition that $Q_{nc} = 0$ at the base of the debris layer. This boundary condition is chosen for its simplicity, and also because it is likely true when the debris near the interface is saturated with meltwater. Q_{nc} is certainly not zero at the debris-air interface, where turbulent and radiative heat fluxes have been measured and may extend down into the upper few centimeters of the debris layer as a result of surface roughness and increased porosity.

We compared the cumulative melt measured at the stake in 21 cm debris to temperature profile P_2020b (22 cm debris thickness), using the following equation to produce an independent estimate of the thermal conductivity k:

$$k = \frac{M \rho_i L_f}{\partial T / \partial z} \tag{5}$$

where M is melt, $\rho_i = 900$ kg m^{-3} is the density of ice and $L_f = 334{,}000$ J kg^{-1} is its latent heat of fusion/melting (Cuffey & Paterson, 2010). This value of k can then be compared with thermal diffusivity κ determined from thermal analysis of P_2020b to constrain ρc. This value of ρc is in turn used to estimate k values from κ for each of the other thermistor profiles.

5. Results

5.1. Debris Thermal Properties

Mean temperature profiles (taken across the entire measurement period) are approximately linear; applying a simple regression on median sensor temperature as a function of depth produces R^2 values between 0.89 (P_2011) and 0.99 (P_2020b) (Figure 2). Calculated temperature gradients range between 0.25°C cm $^{-1}$ (P_2020a) and 0.39°C cm^{-1} (P_2020b), with fitted surface temperatures from 6.5°C (P_2011) to 8.8°C (P_2020a).

Diurnal peaks in debris temperature near the surface (at ~4–6 cm depth) typically range between 20 and 25°C for clear, sunny days and 10°–15°C for cloudy, overcast days. Temperature at greater depths, exhibits diminished diurnal peaks, which arrive progressively later in the day, approaching a limit of constant 0°C temperature at the base of the debris layer.

Partial differentials for temperature are plotted in Figures 3–5. Note that in $\frac{\partial T}{\partial t}$ versus $\frac{\partial^2 T}{\partial z^2}$ space there is the appearance of an elliptical apparent hysteresis in the point clouds. The data generally starts with negative values of $\frac{\partial T}{\partial t}$ and $\frac{\partial^2 T}{\partial z^2}$ at midnight, ascends through the origin in the early morning, reaches a maximum in both parameters during the afternoon, and then descends to their minimum in the late evening before restarting the cycle (Figure 3). As the data descends the $\frac{\partial T}{\partial t}$–$\frac{\partial^2 T}{\partial z^2}$ curve in the late afternoon/evening it does so with markedly elevated values of $\frac{\partial T}{\partial t}$, passing above rather than through the origin and thus inscribing an ellipse rather than a linear point cloud in $\frac{\partial T}{\partial t}$–$\frac{\partial^2 T}{\partial z^2}$ space. This diurnal apparent hysteresis is most evident at a depths of 18 cm for profile P_2020a, and at both sensor depths for P_2011. It is also present for profile P_2020b, but the apparent hysteresis is more subtle ($\frac{\partial T}{\partial t}$ afternoon/evening offset is of lower magnitude).

The magnitude of apparent hysteresis appears to be related to the magnitude of $\frac{\partial T}{\partial z}$ (see color-coding for points in Figures 4 and 5). This is consistent with a full treatment of Equation 2, where $\frac{\partial \kappa}{\partial z}$ is nonnegligible. Applying a multiple linear regression for $\frac{\partial T}{\partial t}$ as a function of $\frac{\partial T}{\partial z}$ and $\frac{\partial^2 T}{\partial z^2}$ we obtain much better fits to data than we do with a single linear regression representing $\frac{\partial T}{\partial t}$ as a function of $\frac{\partial^2 T}{\partial z^2}$ alone (see Figures 4 and 5 vs. Figure 3; results

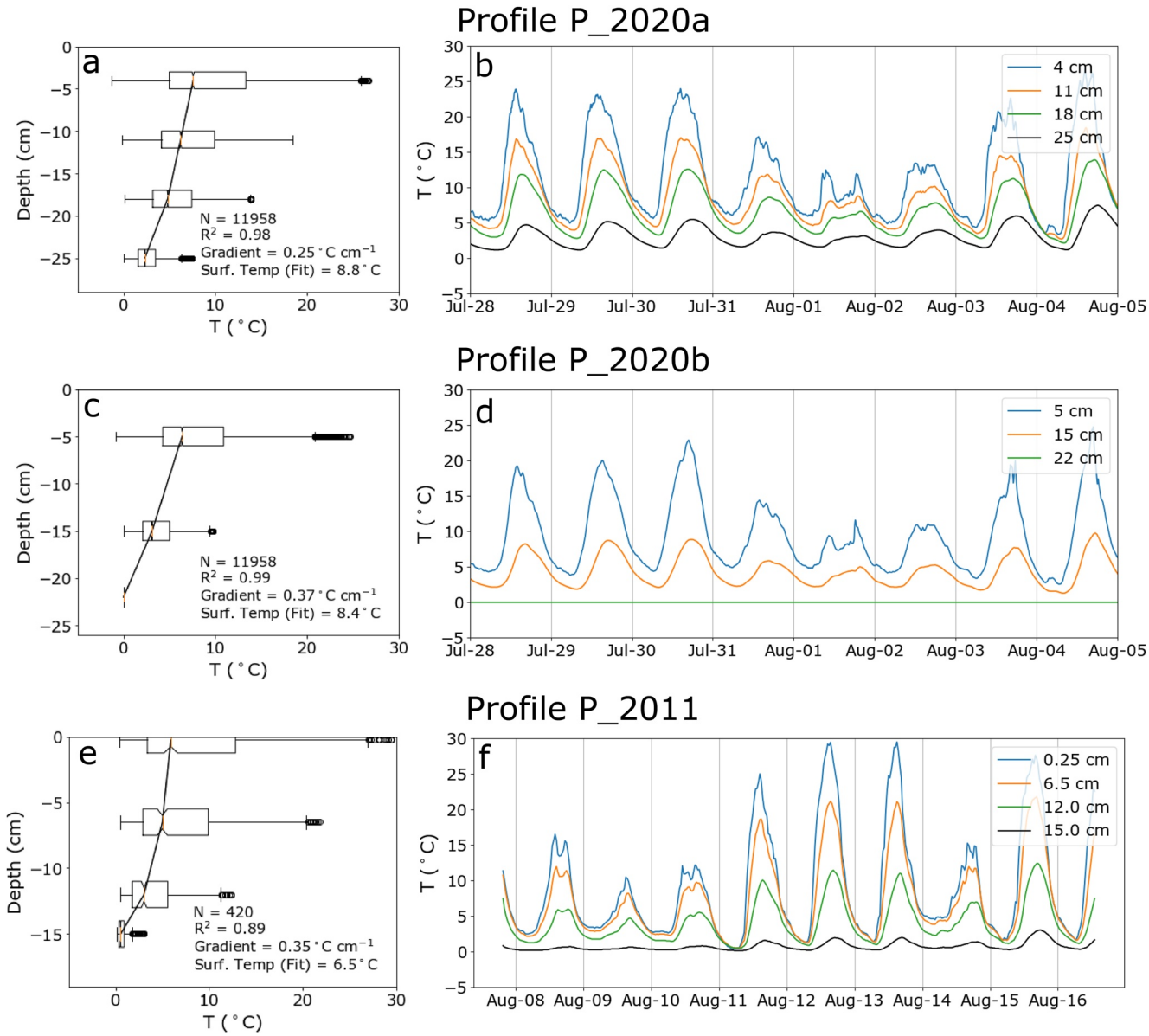

Figure 2. Debris temperature observations for profiles P_2020a (Panels a and b), P_2020b (Panels c and d), and P_2011 (Panels e and f). Left panels show a box and whisker plot for the full statistics of the data set (see Table 1); gradient and surface temperature are constrained from a linear regression of median temperature as a function of depth. Right panels show a sample of the debris temperature time series over the course of 8 days. P_2020a and P_2020b data were acquired at 5 min interval, while P_2011 was acquired at 30 min interval. During the 2020 time series sample, the first three days (28–30 July) are clear and sunny, while the subsequent three days are cloudy (31 July to 2 August).

summarized in Table 2). For most of the data, the inclusion of $\frac{\partial T}{\partial z}$ explains the apparent hysteresis (e.g., see 18 cm depth at P_2020a in Figure 4).

From this method, we constrained values of κ between 2.73 and 9.39×10^{-7} m^2 s^{-1}, values of $\frac{\partial \kappa}{\partial z}$ between -9.00 and 1.60×10^{-8} m^2 s^{-1} cm^{-1}, and coefficients of determination of $R^2 = 0.40$–0.95. Diffusivity values are higher for the upper sensors than the lower sensors in the profiles, and the most extreme values were found in profile P_2011.

Using Equation 5, we were able to calculate the bulk debris layer thermal conductivity $k = 0.638$ W (K m)$^{-1}$ from the cumulative melt at the ablation stake compared to $\partial T/\partial z$ calculated at the base of temperature profile P_2020b (Figure 6). Since $k = \kappa \rho c$, and we determined $\kappa = 5.22 \times 10^{-7}$ m^2 s^{-1} from all data points for profile P_2020b,

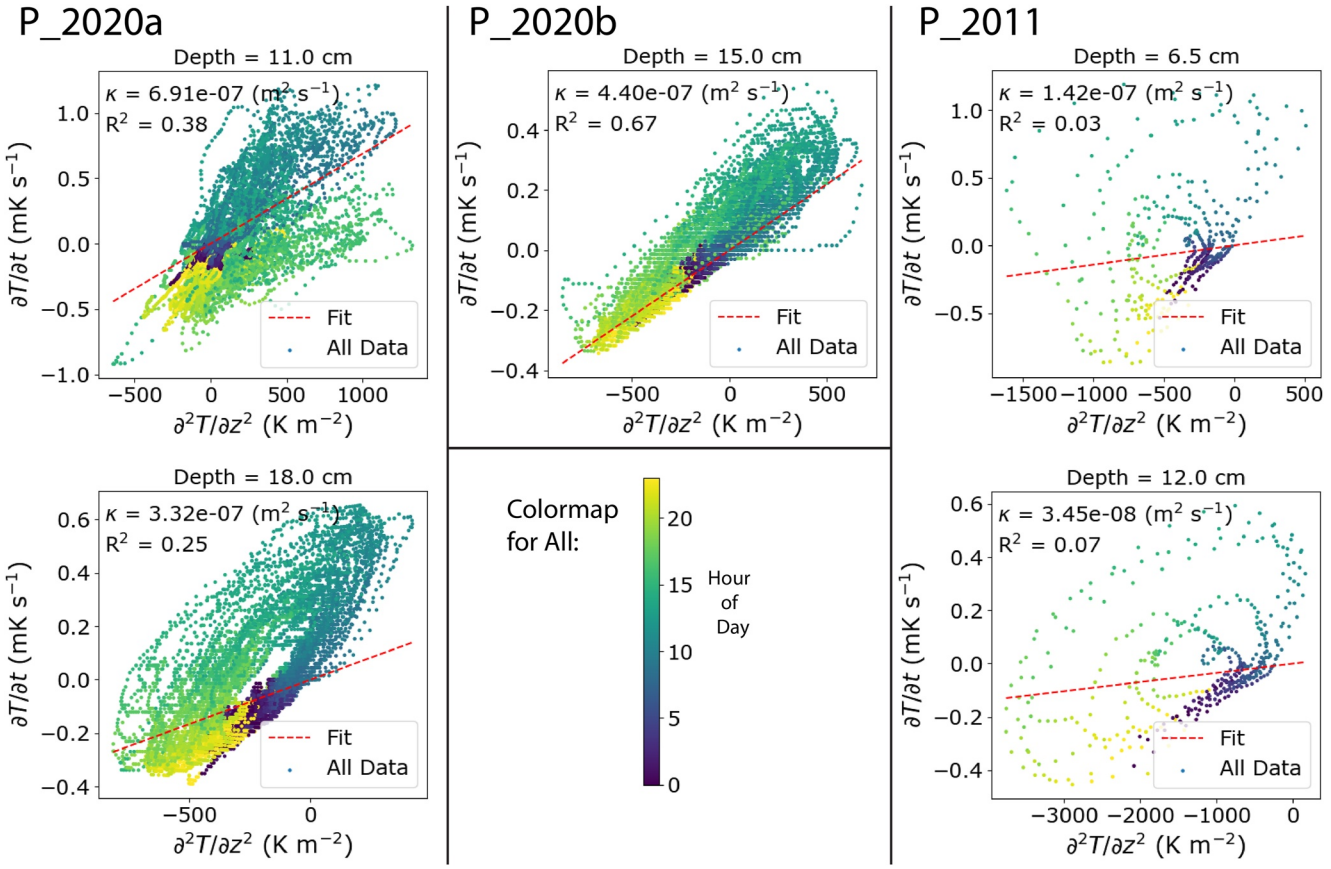

Figure 3. Scatter plots of $\frac{\partial T}{\partial t}$ as a function of $\frac{\partial^2 T}{\partial z^2}$ for each sensor location in the thermistor profiles. The results of linear regressions are shown, giving the determination of κ values. Data points are also color coded to indicate the hour of day between 0:00 and 24:00; note the diurnal apparent hysteresis present at most sensor locations. $\frac{\partial T}{\partial t}$ is expressed in mK s^{-1} to eliminate the need for scientific notation.

we can thus calculate ρc = 1,220,000 J kg m^{-3} K^{-1}. Applying this value of ρc, we estimated thermal conductivity values for all profiles, finding values of k between 0.33 and 1.15 W m^{-1} K^{-1}, summarized in Table 2. Profiles of k values determined at the sensor locations as well as extrapolations based on $\frac{\partial \kappa}{\partial z}$ are shown in Figure 7. As seen in the plots, the gradient in k between the two middle sensor locations in P_2020a and P_2011 matches the trends in $\frac{\partial k}{\partial z}$ determined for the sensor locations. For P_2020a, there is first a trend of increasing k upwards, a leveling off between sensors, and then a trend of decreasing k. For P_2011, there is a continuous trend of increasing k upwards.

The fit to the data, including $\frac{\partial T}{\partial z}$ does not account for all the scatter and hysteresis however. Data at 11 cm depth in profile P_2020a takes a more complicated path through $\frac{\partial T}{\partial t}$–$\frac{\partial^2 T}{\partial z^2}$ space. It first ascends steeply to high $\frac{\partial T}{\partial t}$ in the morning/early afternoon and then descends to lower or negative $\frac{\partial T}{\partial t}$ values for similar values of $\frac{\partial^2 T}{\partial z^2}$ in the evening (see Figure 3). This behavior cannot be explained by a dependence on $\frac{\partial T}{\partial z}$, as shown by the results of the multiple linear regression in Figure 4.

Because this residual hysteresis-like behavior cannot be explained by vertical variation in κ as captured by our multiple linear regression, it implies nonconductive processes at play (see Equation 2), with the magnitude of their influence dependent on the time of day. Thus, we applied our method of quantifying the residual (deviation of data from the results of the multiple linear regression) to determine $\partial Q_{nc}/\partial z$, as described in the following section.

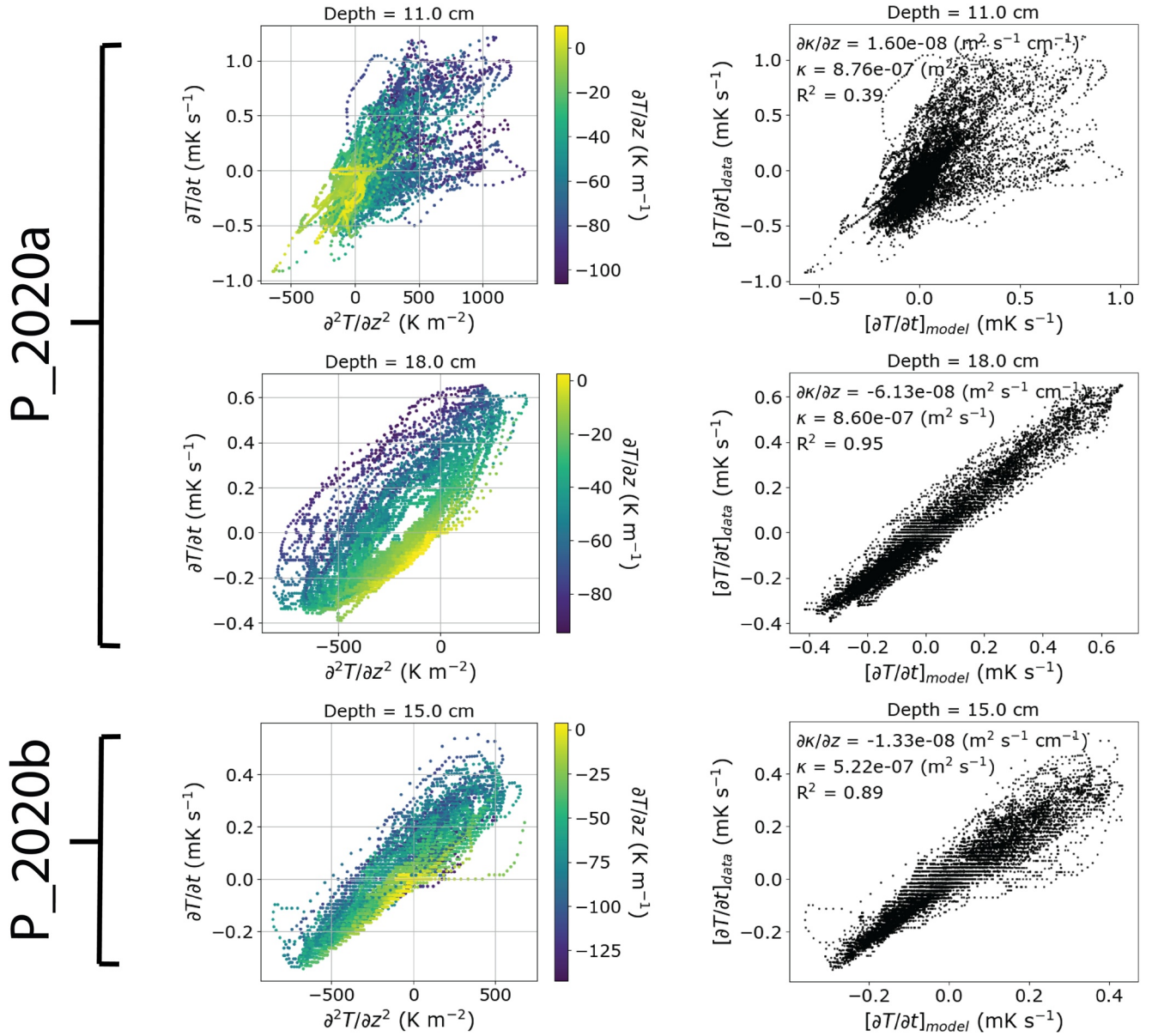

Figure 4. (Left column) Scatter plots of $\frac{\partial T}{\partial t}$ as a function of $\frac{\partial^2 T}{\partial z^2}$ and $\frac{\partial T}{\partial z}$ (displayed by color coding of data points) for debris temperature profiles P_2020a, and P_2020b (Table 1). (Right column) $\left[\frac{\partial T}{\partial t}\right]_{obs}$ plotted against $\left[\frac{\partial T}{\partial t}\right]_{model}$ predicted from the multiple linear regression of $\left[\frac{\partial T}{\partial t}\right]_{obs}$ as a function of $\frac{\partial T}{\partial z}$ and $\frac{\partial^2 T}{\partial z^2}$. Correlation coefficients, effective diffusivity values κ, and their differential $\frac{\partial \kappa}{\partial z}$ as constrained from the linear regression are displayed. Note the circular apparent hysteresis circumscribed through $\frac{\partial T}{\partial t} \times \frac{\partial^2 T}{\partial z^2}$ space at most profile sensor locations, which can be explained by the dependence of $\frac{\partial T}{\partial t}$ on $\frac{\partial T}{\partial z}$ as well.

5.2. Constrained Heat Fluxes

$\partial Q_{nc}/\partial z$ values, derived as a quantification of the residual in measured $\frac{\partial T}{\partial t}$ from the model derived via multiple linear regression as a function of $\frac{\partial T}{\partial z}$ and $\frac{\partial^2 T}{\partial z^2}$ (Equation 3), vary in their magnitude and behavior between sensor locations but tend to exhibit diurnal cycles (Figures 8–10).

At 11 cm depth in Profile P_2020a, there is a pronounced diurnal cycle in $\partial Q_{nc}/\partial z$, a result of the complex apparent hysteresis in $\frac{\partial T}{\partial t}$ versus $\frac{\partial^2 T}{\partial z^2}$ that is not captured by any dependence on $\frac{\partial T}{\partial z}$. At this location, $\partial Q_{nc}/\partial z$ begins rising sharply at 07:00–08:00 hr local time (AKDT and GMT-08:00), reaches its peak between 11:00 and 12:00 hr (at up to >10 W m^{-2} cm^{-1} and diurnal mean 5.5 W m^{-2} cm^{-1}), falls to negative values circa 14:00, and reaches

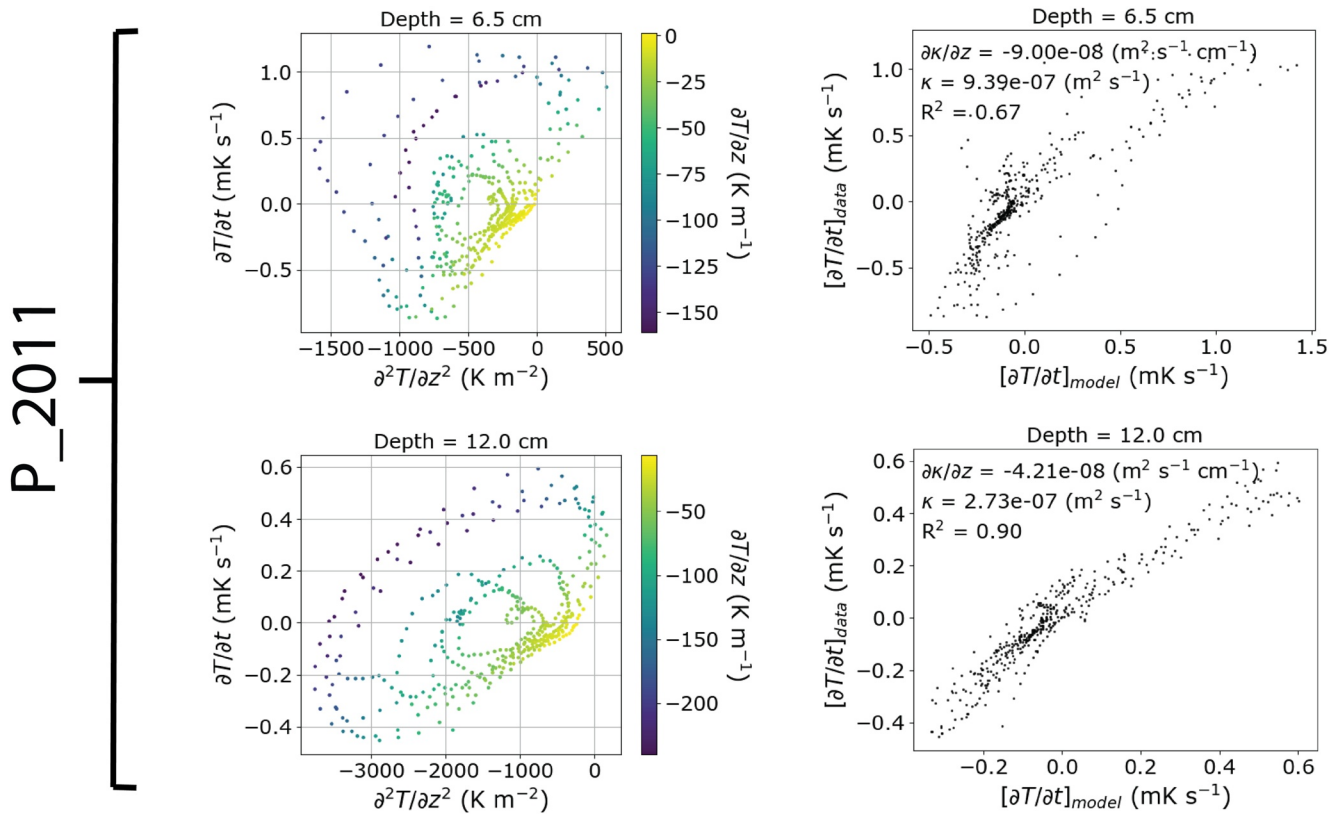

Figure 5. (Left column) Scatter plots of $\frac{\partial T}{\partial t}$ as a function of $\frac{\partial^2 T}{\partial z^2}$ and $\frac{\partial T}{\partial z}$ (displayed by color coding of data points) for debris temperature profiles P_2011 (Table 1). (Right column) $\left[\frac{\partial T}{\partial t}\right]_{obs}$ plotted against $\left[\frac{\partial T}{\partial t}\right]_{model}$ predicted from the multiple linear regression of $\left[\frac{\partial T}{\partial t}\right]_{obs}$ as a function of $\frac{\partial T}{\partial z}$ and $\frac{\partial^2 T}{\partial z^2}$. Correlation coefficients, effective diffusivity values κ and their differential $\frac{\partial \kappa}{\partial z}$ as constrained from the linear regression are displayed. Note the circular apparent hysteresis circumscribed through $\frac{\partial T}{\partial t} \times \frac{\partial^2 T}{\partial z^2}$ space at most profile sensor locations, which can be explained by the dependence of $\frac{\partial T}{\partial t}$ on $\frac{\partial T}{\partial z}$ as well.

its minima at 16:00–17:00 (diurnal mean −4.5 W m^{-2} cm^{-1}) before gradually rising throughout the evening. A far more muted diurnal cycle is present at 18 cm depth, with positive peaks in the afternoon (circa 15:00, diurnal mean 0.8 W m^{-2} cm^{-1}). $\partial Q_{nc}/\partial z$ values are more stochastic at the other sensor locations. They tend to be relatively low for P_2020b (<1–2 W m^{-2} cm^{-1}). For P_2011, values are similarly low at 12 cm but can reach up to ±10 W m^{-2} cm^{-1} at 6.5 cm.

Table 2
Summary of κ Determination Using a Single Linear Regression (Assuming Vertical Variation in κ Is Negligible and ∂κ/∂z = 0) and a Multiple Linear Regression (Assuming Nonzero ∂κ/∂z) Applied to Equation 2

		Single regression		Multiple regression			
Profile	Depth	R^2	κ (m^2 s^{-1})	R^2	κ (m^2 s^{-1})	$\frac{\partial \kappa}{\partial z}$ (m^2 s^{-1} cm^{-1})	k (W m^{-1} K^{-1})
P_2020a	11 cm	0.38	6.91×10^{-7}	0.40	8.76×10^{-7}	1.60×10^{-8}	1.069
	18 cm	0.25	3.32×10^{-7}	0.95	8.60×10^{-7}	-6.13×10^{-8}	1.049
P_2020b	15 cm	0.67	4.40×10^{-7}	0.89	5.22×10^{-7}	-1.33×10^{-8}	0.637
P_2011	6.5 cm	0.04	1.42×10^{-7}	0.67	9.39×10^{-7}	-9.00×10^{-8}	1.146
	12 cm	0.07	3.45×10^{-8}	0.91	2.73×10^{-7}	-4.21×10^{-8}	0.333

Note. The coefficient of determination R^2 for the fits is displayed along with constrained κ and $\partial\kappa/\partial z$. For the multiple linear regression, thermal conductivity k values were derived using ρc = 1,220,000 (J kg)/(m^{-3} K). This value of ρc is consistent with ρ_{rock} = 2,700 kg m^{-3}, porosity ϕ = 40%, and c = 750 J K^{-1}.

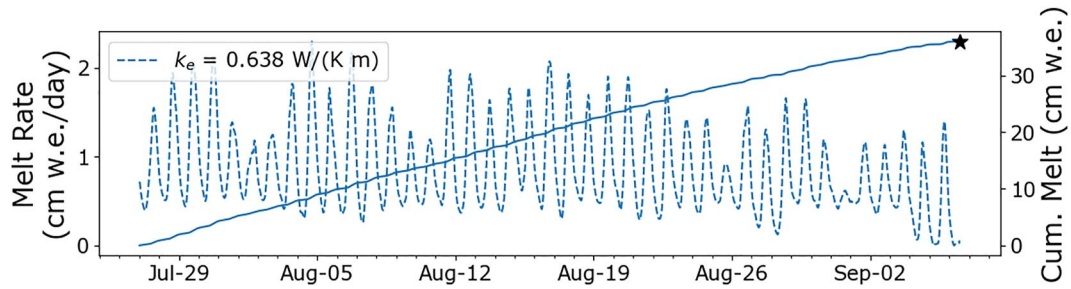

Figure 6. Time series of the modeled sub-debris melt rate and cumulative melt over the period from 27 July to 6 September 2020. The black star refers to the total melt measured by the ablation stake used to constrain k_e using $\partial T/\partial z$ data from temperature profile P_2020b.

The magnitude of $\partial Q_{nc}/\partial z$ on a day-to-day basis is correlated to sky conditions (Figures 8–10). Sunny days with high values of incoming solar radiation result in high values of $\partial Q_{nc}/\partial z$. Profiles P_2020a and P_2011 reach peak $\partial Q_{nc}/\partial z$ values up to >10 W m^{-2} cm^{-1} during sunny days but only <5 W m^{-2} cm^{-1} and <6 W m^{-2} cm^{-1}, respectively, during cloudy days with less incoming solar radiation.

Conductive heat flux Q_c follows a diurnal cycle as the debris layer is heated by solar radiation; sunny days produce elevated values of Q_c while cloudy days produce muted values (Figures 8–10). Values are generally larger at shallower depths and for thinner debris, with near-surface values as high as 208 W m^{-2} (P_2011). At profile P_2020a, however, there is a slight inversion as Q_c at 21.5 cm exceeds that at 14.5 cm. At profile P_2020b, the Q_c cycle has roughly comparable amplitude with delayed timing at depth.

Q_{nc} is lower than Q_c at the same sensor locations. There is a pronounced diurnal cycle for Q_{nc} at 7.5 cm depth in P_2020a, with values rising to a diurnal mean peak of 31 W m^{-2} at 12:00 before falling swiftly to negative values and a diurnal minima of −24 W m^{-2} at 17:00 (Figure 10). This represents roughly 43% and −33% of the diurnal peak in Q_c values for this sensor. This diurnal cycle is more pronounced with higher and sharper peaks on days with sunny sky conditions, similar to the cycle in Q_c. Q_{nc} at 14.5 cm depth exhibits much lower magnitudes, with a diurnal peak of 4 W m^{-2} occurring at 15:00, representing 7% of the diurnal peak in Q_c at that depth.

Q_{nc} values derived for the other profile sensor locations are more stochastic. At P_2020b the largest values, positive or negative, tend to occur in the afternoon. These diurnal peaks rarely exceed 15 W m^{-2}, with a diurnal mean peak of 7 W m^{-2} at 14:00 representing 11% of peak Q_c. At P_2011 shallow Q_{nc} (3.4 cm depth) tends to exhibit strong negative values for sunny days (as low as −60 W m^{-2}; −37 W m^{-2} diurnal mean at 19:00) and positive values for cloudy days (22 W m^{-2} diurnal mean at 14:00). These diurnal extremes represent −31% and 18% of

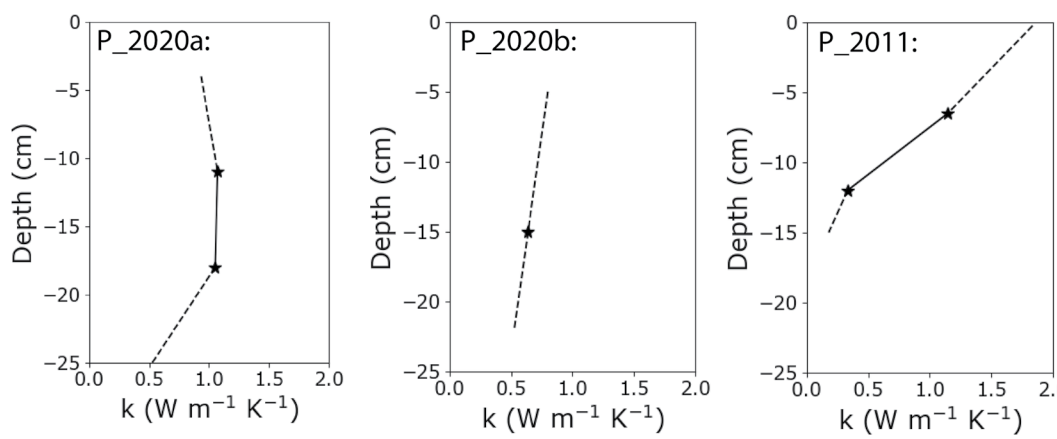

Figure 7. Thermal conductivity k as a function of depth in the thermistor profiles. Values at the thermistor locations are calculated from the determined thermal diffusivity κ multiplied by ρc = 1,220,000 (J kg)/(m^3 K), and displayed as stars. The dashed lines are extrapolated from the determined $\frac{\partial \kappa}{\partial z}$ at the sensor locations.

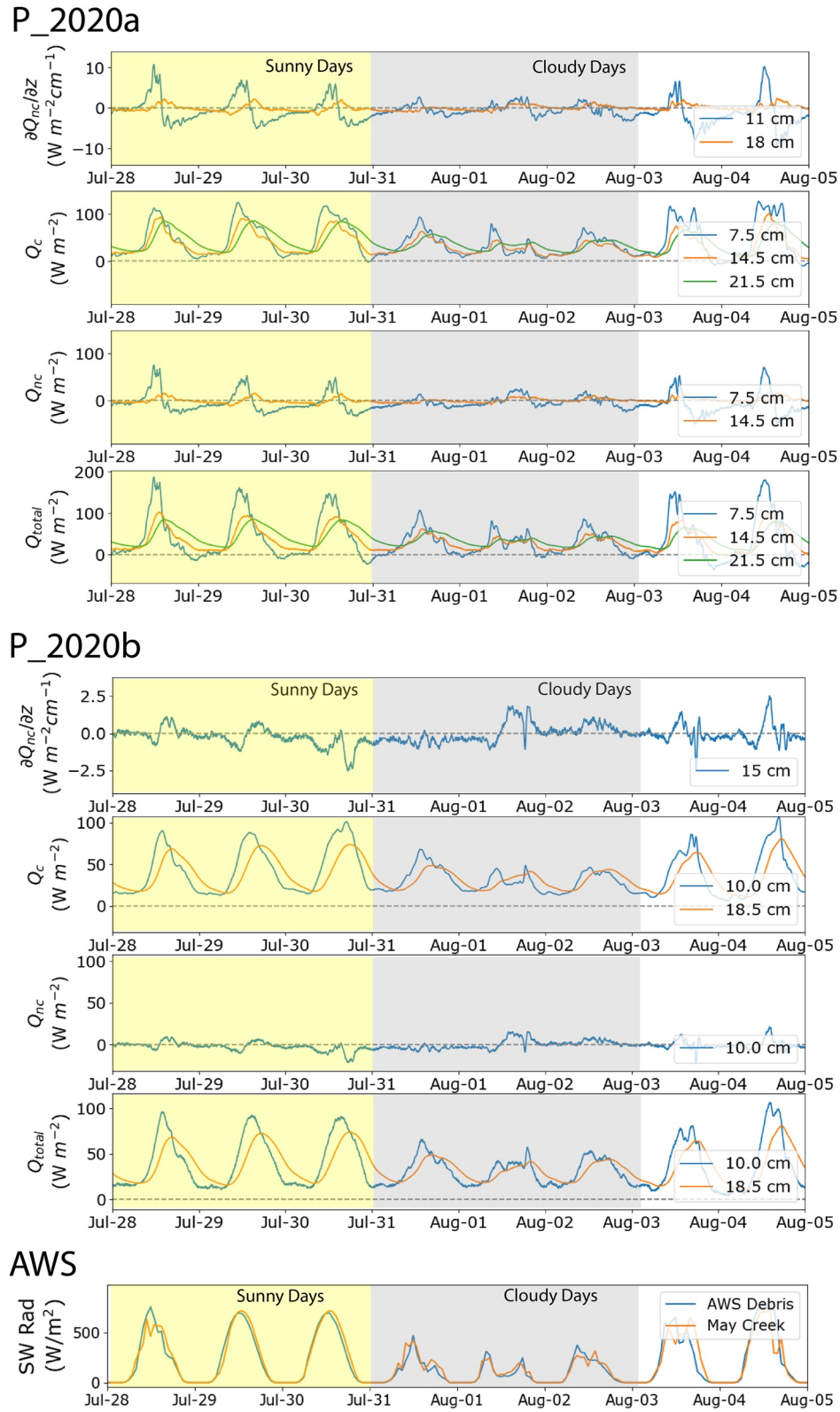

Figure 8. Sample time series for $\partial Q_{nc}/\partial z$, Q_c, Q_{nc}, and Q_{total} at the middle sensors for each temperature profile in summer 2020. Also shown is shortwave radiation measured at the meteorological stations, indicating sunny days (yellow shading) and cloudy days (gray shading).

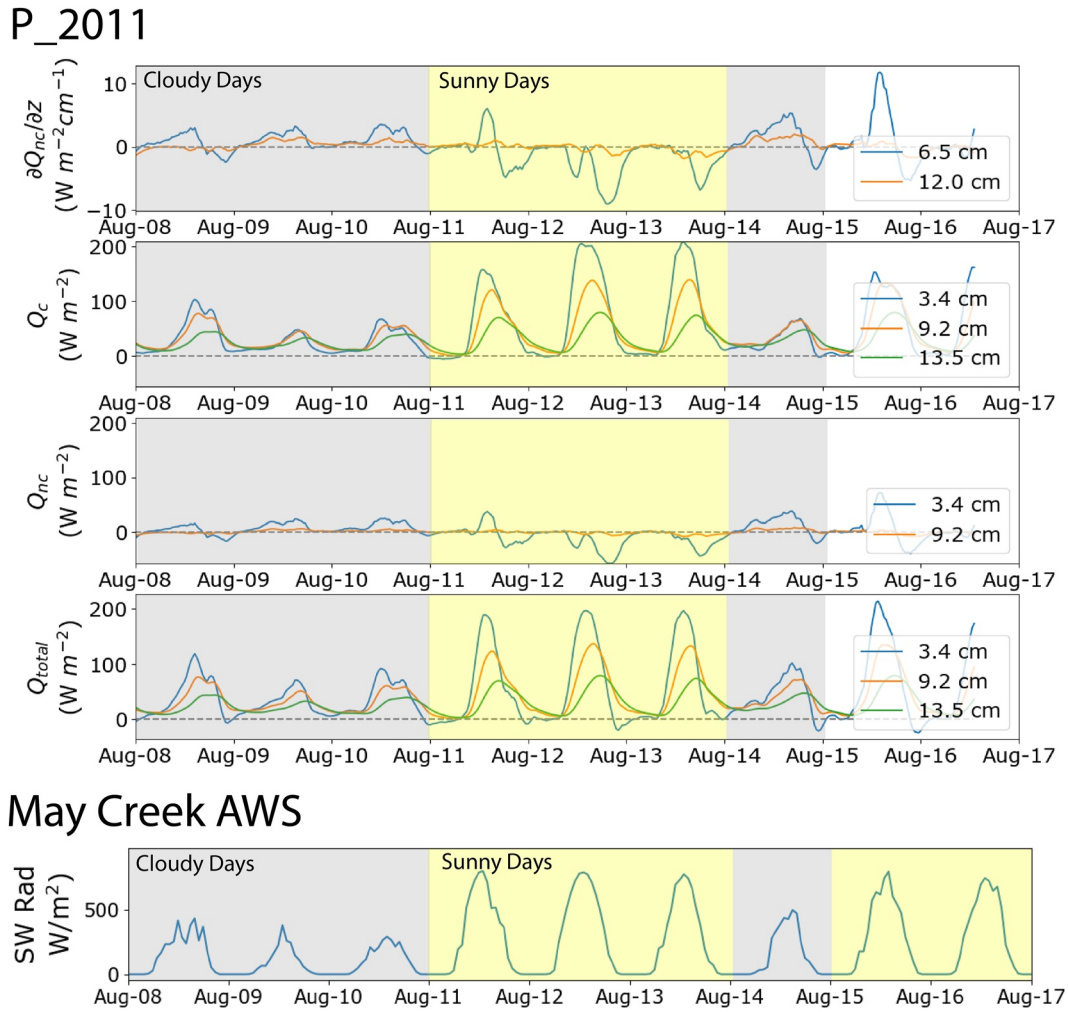

Figure 9. Sample time series for $\partial Q_{nc}/\partial z$, Q_c, Q_{nc}, and Q_{total} at the middle sensors for profile P_2011. Also shown is shortwave radiation measured at the meteorological stations, indicating sunny days (yellow shading) and cloudy days (gray shading).

the mean diurnal peak in Q_c. Q_{nc} values derived at 9.2 cm depth in P_2011 are relatively insignificant, reaching a diurnal peak of 4 W m^{-2}, representing 4.3% of peak diurnal Q_c values.

6. Discussion

6.1. Debris Temperatures and Thermal Properties

The values we found for mean temperature gradient (0.25–0.39°C cm^{-1}) and fitted surface temperature (5.5–8.8°C) are broadly similar to those reported by Rowan et al. (2020) (0.02–0.45°C cm^{-1}; 3.1–9.4°C), a study focused on glaciers in the Everest region. We similarly find that the mean fitted surface temperature is greater for higher debris thickness (as shown in Conway and Rasmussen (2000); Reid et al. (2012); Rowan et al. (2020)), a reasonable finding given the ice-debris interface is at or near 0°C through the melt season.

Our determined values of thermal diffusivity κ range between 2.73×10^{-7} m^2 s^{-2} and 9.39×10^{-7} m^2 s^{-2} (R^2 = 0.40–0.95). By constraining the thermal conductivity through the comparison of temperature gradients to melt rates, we determined ρc = 1,220,000 kg J (m^3 K)$^{-1}$. Standard values used in the literature include ρ_{rock} = 2,700 kg m^{-3}, thermal capacity c = 750 J K^{-1}, and debris porosity ϕ = 30%–33% (Conway & Rasmussen, 2000; Nicholson & Benn, 2012; Rounce et al., 2015). Our value of ρc is consistent with the standard

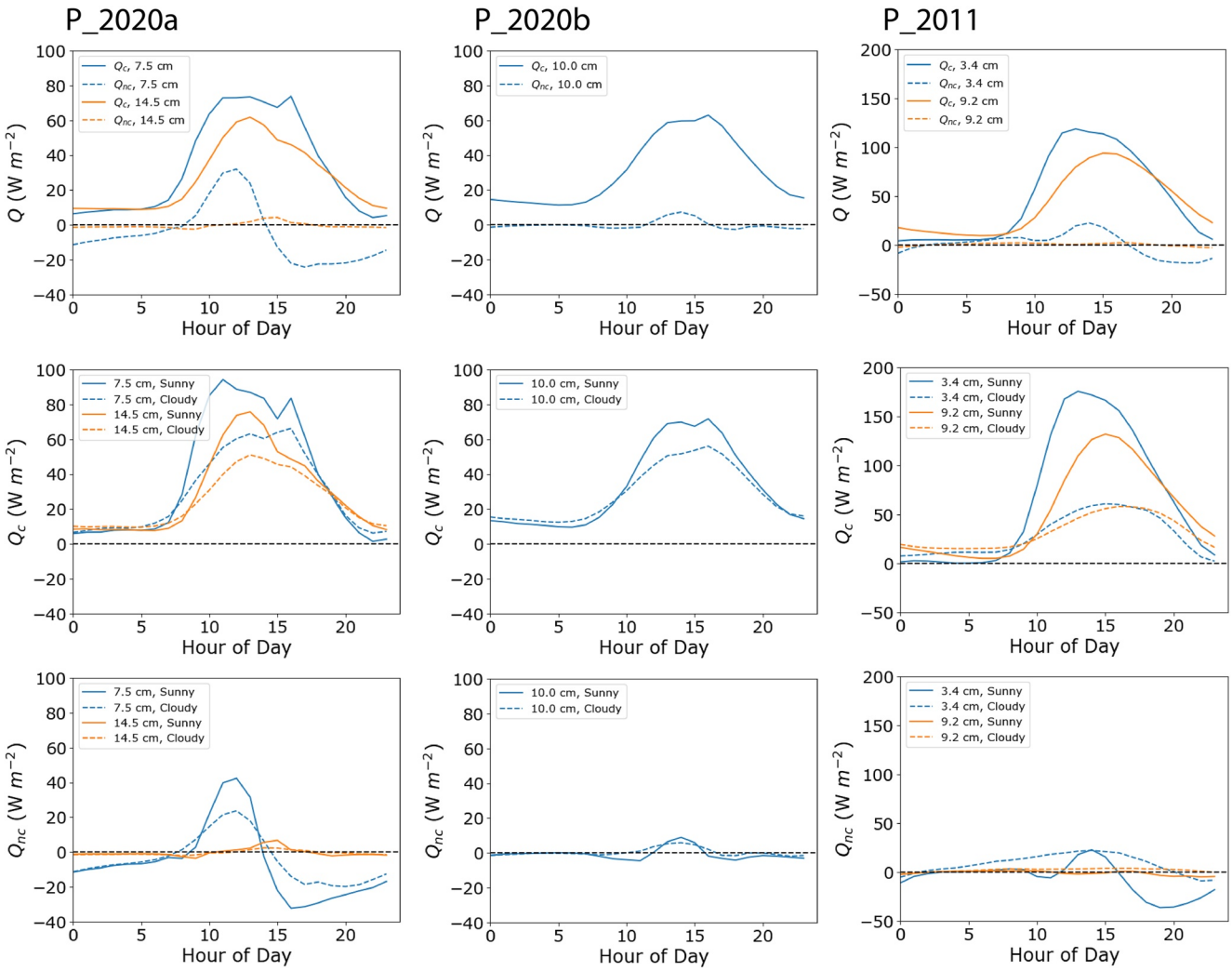

Figure 10. Mean diurnal cycles in heat fluxes for each temperature profile (columns). Top row shows mean diurnal Q_c (solid lines) and Q_{nc} (dashed lines) for all days recorded in Table 1. Middle and bottom rows show Q_c and Q_{nc}, respectively, for sunny days (solid lines) and cloudy days (dashed lines). All plots are at the same scale for ease of intercomparison.

values for ρ_{rock} and c, with $\phi = 40\%$. The agreement between measured melt rates, thermal analysis of temperature data, and standard values found in the literature shows that our derived thermal properties are realistic.

Past studies that have employed a similar analysis found thermal conductivity values between 0.59 and 1.78 W m^{-1} K^{-1} for supraglacial debris in Europe (Nicholson & Benn, 2006; Reid & Brock, 2010; Reid et al., 2012) and 0.47–1.62 W m^{-1} K^{-1} in the Himalaya (Conway & Rasmussen, 2000; Nicholson & Benn, 2012; Rounce et al., 2015), compared to our values of 0.33–1.15 W m^{-1} K^{-1}. Past work on Kennicott Glacier compared debris temperature to measured melt (e.g., using Equation 5) and found values of 0.53–2.16 W m^{-1} K^{-1} (Anderson, Armstrong, Anderson, & Buri, 2021). Thus, all but one of our constrained k values fall within the range found in past work.

The value of $k = 0.33$ W m^{-1} K^{-1} found for P_2011 (12 cm) is lower than found in previous work for supraglacial debris. While our estimation may be affected by uncertainties in thermistor placement or the confounding influence of nonconductive processes, this value is also consistent with that of high porosity dry sand (e.g., Chen, 2008). Thus, it is possible that this site in particular contains debris with uniquely small clast size and/or higher porosity.

6.2. A Novel Approach

Our work in constraining debris thermal properties is novel in that it does not ignore strong vertical variations in debris layer thermal diffusivity; we do this through the inclusion of $\frac{\partial T}{\partial z}$ as well as $\frac{\partial^2 T}{\partial z^2}$ in the multiple linear regression to predict $\frac{\partial T}{\partial t}$. Previous work has only fit $\frac{\partial^2 T}{\partial z^2}$ versus $\frac{\partial T}{\partial t}$ to determine κ (e.g., Nicholson and Benn, 2012). This new approach explains an elliptical apparent counter-clockwise diurnal hysteresis observed in $\frac{\partial T}{\partial t}$ versus $\frac{\partial^2 T}{\partial z^2}$. The effect of this apparent hysteresis would be to confound the previous method for determination of κ by reducing the R^2 value and introduce outliers that skew the fit. As a result, the constrained debris thermal properties would be inaccurate.

The pattern of elliptical apparent hysteresis in $\frac{\partial T}{\partial t}$ versus $\frac{\partial^2 T}{\partial z^2}$ was observed at all temperature profiles (18 cm depth in profile P_2020a, 15 cm depth in P_2020b, and all sensors in P_2011); it is only not clearly present in P_2020a at the 11 cm depth sensor, where a more complex hysteresis pattern occurs. These patterns are most obvious for the 2020 data, which has a 5-min data logging interval over half the summer. However, they are still visible in the P_2011 data, which has a 30-min data logging interval taken only over the course of 8 days.

Examining $\frac{\partial T}{\partial t}$ versus $\frac{\partial^2 T}{\partial z^2}$ scattergrams published in the literature, we find two examples where the point cloud has an elliptical shape similar to Figure 3–for the Khumbu Glacier (Figure 5 in Conway and Rasmussen (2000)) as well as the Ngozumpa Glacier (Figure 7 in Nicholson and Benn (2012)). These studies do not specifically identify the diurnal elliptical path, but they broadly interpret the scatter to be due to nonconductive behavior. We therefore suggest that our novel method may be applied to these data to improve the determination of debris thermal properties as well as produce estimates of nonconductive heat flux.

One limitation to our method is that we consider the coefficients to the fit as independent variables when in fact they are not; $\frac{\partial \kappa}{\partial z}$ is related to κ. Future work should resolve this by solving numerically for $\kappa(z)$ on temperature profiles with a greater number of thermistors. However, our derived $\frac{\partial \kappa}{\partial z}$ values are realistic in context, and we clearly show that they explain the elliptical apparent hysteresis observed in $\frac{\partial T}{\partial t}$ versus $\frac{\partial^2 T}{\partial z^2}$. Further confounding factors, per Equation 2, may include (a) a dependence of $\frac{\partial Q_{nc}}{\partial z}$ on $\frac{\partial T}{\partial z}$, and (b) time-varying $\kappa(z)$ values.

6.3. Nonconductive Heat Fluxes and Their Drivers

There are patterns of hysteresis in $\frac{\partial T}{\partial t}$ versus $\frac{\partial^2 T}{\partial z^2}$ that are not explained by a dependence on vertical variation in debris temperature and thermal properties. This includes the complex diurnal hysteresis observed at P_2020a, 11 cm depth (see Figures 3 and 4). Following Equation 2, this behavior may be explained by the presence of nonconductive heat fluxes Q_{nc}, which are likely to follow a diurnal cycle in shallow debris. Thus we quantified, using the methods described, the nonconductive heat flux Q_{nc}. Because the expression of Q_{nc} in $\frac{\partial T}{\partial t}$ versus $\frac{\partial^2 T}{\partial z^2}$ space is that of an apparent hysteresis, we argue that the concept of fitting an "effective" thermal diffusivity κ_e (e.g., Nicholson & Benn, 2012) to capture nonconductive processes may not do so meaningfully.

Q_{nc} exhibits a diurnal cycle with similar behavior to that of Q_c, with peak mean diurnal values up to 43% or −33% that of Q_c. At greater depth in the debris layer, Q_{nc} becomes more negligible as the debris layer becomes more purely conductive. Thus, nonconductive heat fluxes appear to be driven by near-surface effects including wind, vapor fluxes, and radiation penetrating the upper portion of the debris layer. At greater depth with less access to atmospheric mixing, nonconductive heat fluxes become more insignificant in our thermistor profiles.

More broadly, components of the nonconductive heat flux could include (a) sensible heat transfer due to wind permeating the pore space of the debris, (b) atmospheric radiation penetrating the upper several centimeters, (c) radiative transfer between individual debris grains, (d) convection of air within the debris layer pore space, (e) heat advection as water flows through the debris layer, and (f) latent heat transfer due to evaporation and vapor transport of water in the debris layer.

Wind and radiation penetration of the debris layer may be significant near the surface but is unlikely to extend particularly deep within the debris layer (Evatt et al., 2015); assumed a logarithmic decay of wind speed extending from the rough surface into the debris at depth. These effects may be important for P_2011, where somewhat stochastic patterns emerge in Q_{nc} values at 3.4 cm depth.

Convective heat flux may be a significant fraction of the nonconductive heat flux in debris with sufficient tortuosity and air flow. Convection would aid in heat transfer from the hot surface toward the cooler debris at depth, increasing the energy available for melt. On the other hand, large-scale convective cooling similar to that observed in rock glaciers (Delaloye & Lambiel, 2005; Wicky & Hauck, 2020) is not expected at this site for several reasons. First, our analysis covers only the summer months with a focus on diurnal timescales and melt. Second, convection is unlikely to occur at a large scale on Kennicott Glacier as its debris layer is generally much thinner than that of a rock glacier (tens of centimeters vs. meters) and drapes a high-roughness glacier surface with a low overall large-scale slope as opposed to the steep alpine slopes occupied by rock glaciers.

Heat advection through horizontal water flow within the debris is also thought to be negligible. If present, there should be evidence for an increase in nonconductive heat flux toward the base of the debris layer where the water drains; however, this is not observed. Additionally, the high surface roughness of Kennicott Glacier combined with the selection of sites for debris thermistor profiles reduces the potential for significant runoff within the debris layer.

Latent heat flux is likely a strong driver of nonconductive heat fluxes in the debris layer. Moisture content in the debris layer is enhanced at its base by sub-debris melt during the day. This moisture is wicked upward through the debris layer via capillary action, a process that occurs as sub-debris melt extends through the evening. This upward wicking of moisture is itself dependent on the debris layer tortuosity, a function of clast size distribution, sorting, and porosity. Capillary rising on the order of several centimeters is expected for fine gravels with 2–5 mm clast size (Lohman, 1972). We observed evidence for capillary action while digging supraglacial debris pits, in that a significant fraction of the debris depth was moistened but not saturated (see Figure 1b). The shallow/near surface portion of the wet debris layer is then primed to effectively dry out the following day when it is warmed up by positive surface energy balance preceding the diurnal rise in sub-debris melt rates and resultant moisture source from below. The wetting/drying front and associated peak in latent heat fluxes thus oscillate up and down through the debris layer on a diurnal cycle. The base of the debris layer does not completely dry out during the ablation season on the basis of near-continuous (if highly variable) melting, as well as the observation that all debris pits dug during fieldwork at many times of day in the ablation season exhibited some moisture within them. Because of water's high latent heat of vapourization (L_v = 2,260 kJ m^{-1}), even a comparatively small vapor flux can lead to a large latent heat flux and a resultant reduction in melt.

This interpretation is supported by the fact that our derived $\partial Q_{nc}/\partial z$ and Q_{nc} values (a) follow diurnal cycles and (b) reach higher values for sunny days than for cloudy days. Net shortwave radiation is a major driver of heat flux through the debris layer and resultant sub-debris melt rates (e.g., Steiner et al., 2018; Rounce et al., 2015), which in turn determines melt water and heat availability to drive latent heat exchange, which we measure in this work as Q_{nc}. The drop-off in Q_{nc} values compared to Q_c in the afternoon/evening may be related to the drying of the debris layer at a given depth (P_2020a and 7.5 cm)–as the wetting front recedes, the magnitude of the vapor gradient at that location will be reduced. The switch to negative values of Q_{nc} we interpret to indicate other processes dominating as latent heat is reduced. This would include air convection and intergrain radiative transfer, which reverses the sign of the heat flux and contributes to heat available for melt. While it is possible that condensation occurs, representing a change in sign of the latent heat flux, we find this unlikely in the afternoon and early evening when the debris is still heated.

The strong gradient in thermal conductivity giving higher values near the debris surface at P_2011 (Figure 7) is not necessarily expected for a debris layer exhibiting wet sediments towards its base, which would increase the bulk thermal conductivity. This may indicate that latent heat flux is not a strong influence on P_2011, or that other debris properties such as clast lithology/stratigraphy may hold a stronger influence. In any case, the debris layer need not be totally saturated, but only contain some moisture content for the activation of latent heat transfer.

In the profile P_2020a the nonconductive heat flux at depth (14.5 cm) lags behind the shallow heat flux (7.5 cm) (Figure 8), indicating that it propagates from the debris surface down towards the ice-debris interface. As Q_{nc} peaks at depth, it falls to negative values near the surface, and during the late afternoon/early evening, the values for $\partial Q_{nc}/\partial z$ are positive at 18 cm and negative at 11 cm, which indicates that a peak in Q_{nc} occurs between 11 and 18 cm depth at this time. Such a peak in Q_{nc} may represent a wetting front—a boundary between the drier upper part of the debris layer and the wetter lower part of the debris layer where latent heat fluxes are maximized. As evaporation occurs first for shallower depths in the debris layer, the nonconductive heat flux thus propagates downwards, and the sign of the heat flux is reversed as the interface between wet and dry passes through a

given horizon in the debris layer. The downward motion of the wetting front is then halted by replenished melt water as a result of diurnal sub-debris melt. This is conceptually consistent with the model presented by Collier et al. (2014).

6.4. Implications for Future Work

Interpretation of our results would be improved and our hypotheses tested by more complementary in situ measurements as well as through advances in modeling heat and water liquid/vapor flux through the supraglacial debris layer. Measurements of time-varying moisture content and relative humidity in the debris layer would be valuable to test our interpretation that latent heat flux dominates nonconductive fluxes. These measurements are challenging to make due to the high porosity, heterogeneity, and instability of supraglacial debris layers. Several models published in the literature have addressed the effect of convection or debris layer moisture content on energy balance and heat flux through the debris layer, but they would each require some modification to test our hypotheses, and some nonconductive processes remain unaddressed in any models. The processes we recommend should be focused on in future model studies include, in order of relative importance: (a) latent heat flux, (b) convection (sensible heat flux), (c) heat advection due to water flux, and (d) radiative transfer between grains in the supraglacial debris layer.

The work of Giese et al. (2020) is promising; their model uses sub-debris melt as an input to predict debris layer moisture content in a modified soil moisture/energy balance model. Their work displayed diurnal cycles of moisture rising within the debris layer from glacier melt and falling as a result of latent heat exchange and runoff, consistent with the interpretation we applied to our results. Giese et al. (2020) showed that a fully saturated debris layer significantly reduces melt relative to a dry debris layer, but that with their chosen set of model parameters (including runoff timescale), the partially saturated case produces very similar results to the dry case. This may be because the model does not account for latent heat fluxes within the porous debris layer, only at the surface.

Collier et al. (2014) modeled the water level in the debris layer in order to estimate latent heat fluxes, evaluated at the water level for any given moment in time. However, modeled melt was not used as a direct input to water content, but rather the level was fixed at 1 cm during melt periods. Upward wicking of water via capillary action was not considered, which would increase water surface area and latent heat flux. As a result, the modeled water level largely reflects inputs from precipitation, surface snow melt, and the drying thereof. Therefore, it is not possible to directly and quantitatively compare their work to our conclusions. The Giese et al. (2020) model improved on the work of Collier et al. (2014) by capturing capillary action and the introduction of melt water, but does not evaluate latent heat fluxes within debris. Capturing both of these processes would be necessary for a model to address our hypothesis.

Thus, accounting for latent heat fluxes, within debris in the context of the Giese et al. (2020) model or a similar moisture content debris model is the next logical step to testing our hypotheses and advancing our understanding of heat flux in supraglacial debris. Such a model could be constrained by the data analysis and nonconductive heat flux constraints that we present in this work. The model can then determine if latent heat flux is the primary driver of observed nonconductive heat flux as we hypothesize.

In addition to latent heat fluxes we may also consider including sensible heat fluxes for air convection in debris, as has been done in an analytical model by Evatt et al. (2015) and in a numerical model for alpine talus by Wicky and Hauck (2020). Radiation between blocks may also be considered (M. Scherler et al., 2014), as well as advection of heat through liquid water flow. A full treatment of all these effects modeled for debris of different tortuosities and other physical properties may permit us to determine the relative importance of each nonconductive process in contributing to supraglacial debris heat flux under different conditions. The results of such work may lead to predictions as to the melt-reducing effects of a debris layer as a function of its grain size distribution, tortuosity, and hydrologic context in addition to its thickness and thermal diffusivity.

Nonconductive processes that could increase energy available for melting include downwelling radiation penetration of the upper few centimeters of the debris layer, radiative heat transfer between individual debris clasts, and sensible heat fluxes due to convection of air in the upper debris layer. The latter two may be the process occurring to produce negative heat flux values observed in the afternoon at Profile P_2020a, as well as negative values at P_2011.

The degree to which rocky supraglacial debris modifies melt relative to clean ice is described by the well-known Østrem curve (Østrem, 1959). Thin debris enhances melt due to increased albedo, but for sufficiently thick debris (on the order of several centimeters), sub-debris melt rates are significantly attenuated compared to clean ice melt rates. This has been attributed to the ability of heated debris to more effectively emit heat through outgoing long wave radiation and negative sensible heat fluxes (Fyffe et al., 2014; Reid et al., 2012), as well as the limitations that heat conduction through a thicker debris layer place on the diurnal forcing of solar radiation (Reid & Brock, 2010). Our work highlights that nonconductive heat flux within the pore space is another mechanism by which supraglacial debris modulates sub-debris melt rates. With hourly Q_{nc} values derived at up to 43% that of Q_c, nonconductive processes such as subsurface latent, sensible, and radiative heat fluxes can play a major role in determining sub-debris melt rates.

Constraining the boundary conditions to explicitly solve Equation 4 remains a challenge. While our imposed boundary condition of $Q_{nc} = 0$ at the debris-boundary interface is a good starting point, it may be a poor assumption if sufficient latent heat exchange occurs at this depth. This may indeed be the case for the onset of sub-debris melt early in the day, as the wetting front is still at its minimum height in the debris layer and has not yet wicked upwards toward its near-surface peak.

A possible future solution is the inclusion of a heat plate to supplement the temperature profile, providing a boundary layer constraint on Q which can then be used to further constrain the solution for Q_{nc}. Heat flux plates are commonly used for soil studies and have been used to compare with heat flux analysis from temperature and water content sensor profiles (Evett et al., 2012). Indeed, the combination of one or more heat plates with a temperature sensor profile could provide a powerful new instrument setup to measure conductive and nonconductive heat fluxes in porous, variably wet media such as the supraglacial debris layer.

7. Conclusions

We developed a technique to apply a more complete treatment of the heat conservation and conduction equations to temperature profile data in supraglacial debris, which improves the determination of debris thermal properties as well as quantifies the conductive and nonconductive heat fluxes, Q_c and Q_{nc}, individually. We find that both heat fluxes have a strong diurnal signal that lags behind solar radiation, the primary driver of diurnal variations in sub-debris melt rates. In addition, these values are generally larger in magnitude for sunny days (high energy input into the system) than for cloudy days (lower energy input into the system).

Nonconductive heat fluxes can peak at 43% of conductive heat fluxes, but with a diurnal cycle that exhibits a steeper drop-off from peak values in the afternoon/evening. We interpret these nonconductive heat fluxes as being driven by latent heat fluxes from evaporation of moisture in the debris layer. This work thus shows that nonconductive heat flux within the supraglacial debris layer is an important component of surface energy balance for debris-covered glaciers, which should be investigated in more detail and incorporated into energy balance models.

Future work should include an analysis of data for different glaciers and locations on glaciers, sampling debris layers of differing porosity, clast size, stratigraphy/sorting, and other properties. Some debris layers may be more amenable to upward wicking of meltwater, or through higher porosity, allow more air flow and thus latent heat exchange, favoring higher levels of Q_{nc}. Importantly, debris layers that are more effective at facilitating latent heat exchanges may be more effective at reducing sub-debris melt rates.

Data Availability Statement

Data and the code developed to produce the plots are available together at Petersen (2022) (https://zenodo.org/record/6574222).

Acknowledgments
Eric Petersen and Regine Hock were supported by NSF Award 1917536 (GLD). Leif Anderson acknowledges support from a 2011 Muire Science and Learning Center Fellowship, NSF DGE-1144083 (GRFP), and funding from the European Union's Horizon 2020 research and innovation program under grant agreements No. 759639 and 851614. Thanks to Martin Truffer for the loan of sensors and field equipment. The authors acknowledge the invaluable help of field volunteers including Jason Geck, Nicole Trenholm, Andrew Johnson, Ruitang Yang, Brooke Kubby, and David Harvey. The authors extend a thank you to the Wrangell Mountains Center staff and its executive director, Jon Erdman, for providing logistical help during fieldwork. The authors also thank National Park Service staff Michael Loso and Mark Miller for their support.

References

Anderson, L. S., Armstrong, W. H., Anderson, R. S., & Buri, P. (2021). Debris cover and the thinning of Kennicott Glacier, Alaska: In situ measurements, automated ice cliff delineation and distributed melt estimates. *The Cryosphere*, *15*(1), 265–282. https://doi.org/10.5194/tc-15-265-2021

Anderson, L. S., Armstrong, W. H., Anderson, R. S., Scherler, D., & Petersen, E. (2021). The causes of debris-covered glacier thinning: Evidence for the importance of ice dynamics from Kennicott Glacier, Alaska. *Frontiers of Earth Science*, *9*. https://doi.org/10.3389/feart.2021.680995

Bartlett, O. T., Ng, F. S. L., & Rowan, A. V. (2020). Morphology and evolution of supraglacial hummocks on debris-covered Himalayan glaciers. *Earth Surface Processes and Landforms*, *46*(3), 525–539. https://doi.org/10.1002/esp.5043

Bhushan, S., Syed, T. H., Arendt, A. A., Kulkarni, A. V., & Sinha, D. (2018). Assessing controls on mass budget and surface velocity variations of glaciers in Western Himalaya. *Scientific Reports*, *8*(1), 8885. https://doi.org/10.1038/s41598-018-27014-y

Bonekamp, P. N. J., Heerwaarden, C. C. V., Steiner, J. F., & Immerzeel, W. W. (2020). Using 3D turbulence-resolving simulations to understand the impact of surface properties on the energy balance of a debris-covered glacier. *The Cryosphere*, *14*(5), 1611–1632. https://doi.org/10.5194/tc-14-1611-2020

Boulton, G. S. (1978). Boulder shapes and grain-size distributions of debris as indicators of transport paths through a glacier and till Genesis. *Sedimentology*, *25*(6), 773–799. https://doi.org/10.1111/j.1365-3091.1978.tb00329.x

Bozhinskiy, A. N., Krass, M. S., & Popovnin, V. V. (1986). Role of debris cover in the thermal physics of glaciers. *Journal of Glaciology*, *32*(111), 255–266. https://doi.org/10.3189/S0022143000015598

Chen, S. X. (2008). Thermal conductivity of sands. *Heat and Mass Transfer*, *44*(10), 1241–1246. https://doi.org/10.1007/s00231-007-0357-1

Collier, E., Nicholson, L. I., Brock, B. W., Maussion, F., Essery, R., & Bush, A. B. G. (2014). Representing moisture fluxes and phase changes in glacier debris cover using a reservoir approach. *The Cryosphere*, *8*(4), 1429–1444. https://doi.org/10.5194/tc-8-1429-2014

Conway, H., & Rasmussen, L. A. (2000). Summer temperature profiles within supraglacial debris on Khumbu Glacier, Nepal. Debris-Covered Glaciers. In *Proceedings of a workshop held at Seattle* (Vol. *264*, pp. 89–97). Retrieved from http://hydrologie.org/redbooks/a264/iahs_264_0089.pdf

Cuffey, K. M., & Paterson, W. S. B. (2010). *The physics of glaciers* (4th ed.). Academic Press. Retrieved from https://www.cambridge.org/core/journals/journal-of-glaciology/article/km-cuffey-and-wsb-paterson-2010-the-physics-of-glaciers-fourth-edition-amsterdam-etc-academic-press-704pp-isbn10-0123694612-isbn13-9780123694614-hardback-60997195us9995/A0CEC70A6DEED2873B685D9AE9C483F9

Das, I., Hock, R., Berthier, E., & Lingle, C. S. (2014). 21st-century increase in glacier mass loss in the Wrangell Mountains, Alaska, USA, from airborne laser altimetry and satellite stereo imagery. *Journal of Glaciology*, *60*(220), 283–293. https://doi.org/10.3189/2014JoG13J119

Delaloye, R., & Lambiel, C. (2005). Evidence of winter ascending air circulation throughout talus slopes and rock glaciers situated in the lower belt of alpine discontinuous permafrost (Swiss Alps). *Norsk Geografisk Tidsskrift - Norwegian Journal of Geography*, *59*(2), 194–203. https://doi.org/10.1080/00291950510020673

Dolgushin, L. (1972). Vliyaniye eolovoy zapylennosti lednikov i poverkhnostnoy moreny na tayaniye lednikov Sredney Azii. [The influence of Aeolian dusting of glaciers and superficial moraine on glacier thawing in Central Asia). *Materialy Glyatsiologicheskikh Issledovaniy, Khronika Obsuzhdeniya*, *20*, 108–116.

Evatt, G. W., Abrahams, I. D., Heil, M., Mayer, C., Kingslake, J., Mitchell, S. L., et al. (2015). Glacial melt under a porous debris layer. *Journal of Glaciology*, *61*(229), 825–836. https://doi.org/10.3189/2015JoG14J235

Evett, S. R., Agam, N., Kustas, W. P., Colaizzi, P. D., & Schwartz, R. C. (2012). Soil profile method for soil thermal diffusivity, conductivity and heat flux: Comparison to soil heat flux plates. *Advances in Water Resources*, *50*, 41–54. https://doi.org/10.1016/j.advwatres.2012.04.012

Fyffe, C. L., Reid, T. D., Brock, B. W., Kirkbride, M. P., Diolaiuti, G., Smiraglia, C., & Diotri, F. (2014). A distributed energy-balance melt model of an alpine debris-covered glacier. *Journal of Glaciology*, *60*(221), 587–602. https://doi.org/10.3189/2014JoG13J148

Giese, A., Boone, A., Wagnon, P., & Hawley, R. (2020). Incorporating moisture content in surface energy balance modeling of a debris-covered glacier. *The Cryosphere*, *14*(5), 1555–1577. https://doi.org/10.5194/tc-14-1555-2020

Hénot, M., Plihon, N., & Taberlet, N. (2021). Onset of glacier tables. *Physical Review Letters*, *127*(10), 108501. https://doi.org/10.1103/PhysRevLett.127.108501

Herreid, S., & Pellicciotti, F. (2018). Automated detection of ice cliffs within supraglacial debris cover. *The Cryosphere*, *12*(5), 1811–1829. https://doi.org/10.5194/tc-12-1811-2018

Inoue, J., & Yoshida, M. (1980). Ablation and heat exchange over the Khumbu Glacier. *Journal of the Japanese Society of Snow and Ice*, *41*(Special), 26–33. https://doi.org/10.5331/seppyo.41.Special_26

Kayastha, R. B., Takeuchi, Y., Nakawo, M., & Ageta, Y. (2000). Practical prediction of ice melting beneath various thickness of debris cover on Khumbu Glacier, Nepal, using a positive degree-day factor, 11.

Khodakov, V. (1972). Raschet i prognoz ablyatsii morenosoderzhashchego l'da. [Calculation and prognosis of debris-containing ice ablation). *Materialy Glyatsiologicheskikh Issledovaniy, Khronika Obsuzhdeniya*, *20*, 215–218.

Lejeune, Y., Bertrand, J.-M., Wagnon, P., & Morin, S. (2013). A physically based model of the year-round surface energy and mass balance of debris-covered glaciers. *Journal of Glaciology*, *59*(214), 327–344. https://doi.org/10.3189/2013JoG12J149

Lohman, S. W. (1972). *Ground-water hydraulics*. (Tech. Rep. No. 708). U.S. Geological Survey. https://doi.org/10.3133/pp708

MacKevett, E. M. (1978). Geologic map of the McCarthy quadrangle.

Mattson, L., Gardner, J., & Young, G. (1993). Ablation on debris covered glaciers: An example from the Rakhiot glacier, Punjab, Himalaya. *International Association of Hydrological Sciences*, *218*, 298–296.

Mihalcea, C., Mayer, C., Diolaiuti, G., D'Agata, C., Smiraglia, C., Lambrecht, A., et al. (2008). Spatial distribution of debris thickness and melting from remote-sensing and meteorological data, at debris-covered Baltoro glacier, Karakoram, Pakistan. *Annals of Glaciology*, *48*, 49–57. https://doi.org/10.3189/172756408784700680

Mölg, N., Ferguson, J., Bolch, T., & Vieli, A. (2020). On the influence of debris cover on glacier morphology: How high-relief structures evolve from smooth surfaces. *Geomorphology*, *357*, 107092. https://doi.org/10.1016/j.geomorph.2020.107092

Morard, S., Delaloye, R., & Lambiel, C. (2010). Pluriannual thermal behavior of low elevation cold talus slopes in Western Switzerland. *Geographica Helvetica*, *65*(2), 124–134. https://doi.org/10.5194/gh-65-124-2010

Nicholson, L., & Benn, D. I. (2006). Calculating ice melt beneath a debris layer using meteorological data. *Journal of Glaciology*, *52*(178), 463–470. https://doi.org/10.3189/172756506781828584

Nicholson, L., & Benn, D. I. (2012). Properties of natural supraglacial debris in relation to modelling sub-debris ice ablation. *Earth Surface Processes and Landforms*, *38*(5), 490–501. https://doi.org/10.1002/esp.3299

Nicholson, L., McCarthy, M., Pritchard, H. D., & Willis, I. (2018). Supraglacial debris thickness variability: Impact on ablation and relation to terrain properties. *The Cryosphere*, *12*(12), 3719–3734. https://doi.org/10.5194/tc-12-3719-2018

Nicholson, L., & Stiperski, I. (2020). Comparison of turbulent structures and energy fluxes over exposed and debris-covered glacier ice. *Journal of Glaciology*, *66*(258), 543–555. https://doi.org/10.1017/jog.2020.23

Østrem, G. (1959). Ice Melting under a thin layer of moraine, and the existence of ice cores in moraine ridges. *Geografiska Annaler*, *41*(4), 228–230. https://doi.org/10.1080/20014422.1959.11907953

Petersen, E. (2022). ericivanpetersen/supraglacial_debris_heat_flux_jgr: JGR paper revision [Software and Data]. Zenodo. https://doi.org/10.5281/zenodo.6574222

Reheis, M. J. (1975). Source, transportation and deposition of debris on Arapaho glacier, front range, Colorado, U.S.A. *Journal of Glaciology*, *14*(72), 407–420. https://doi.org/10.3189/S0022143000021936

Reid, T. D., & Brock, B. W. (2010). An energy-balance model for debris-covered glaciers including heat conduction through the debris layer. *Journal of Glaciology*, *56*(199), 903–916. https://doi.org/10.3189/002214310794457218

Reid, T. D., Carenzo, M., Pellicciotti, F., & Brock, B. W. (2012). Including debris cover effects in a distributed model of glacier ablation. *Journal of Geophysical Research*, *117*(D18). https://doi.org/10.1029/2012JD017795

RGI Consortium. (2017). *Randolph Glacier inventory - a dataset of global glacier outlines: Version 6.0: Technical report*. (Tech. Rep.). Global Land Ice Measurements from Space. https://doi.org/10.7265/N5-RGI-60

Rickman, R. L., & Rosenkrans, D. S. (1997). *Hydrologic conditions and hazards in the Kennicott river basin, (Tech. Rep. No. Water-Resources investigations report 96-4296)*. United States Geological Survey.

Roth, K., & Boike, J. (2001). Quantifying the thermal dynamics of a permafrost site near Ny-Ålesund, Svalbard. *Water Resources Research*, *37*(12), 2901–2914. https://doi.org/10.1029/2000WR000163

Rounce, D. R., Hock, R., McNabb, R. W., Millan, R., Sommer, C., Braun, M. H., et al. (2021). Distributed global debris thickness estimates reveal debris significantly impacts glacier mass balance. *Geophysical Research Letters*, *48*(8), e2020GL091311. https://doi.org/10.1029/2020GL091311

Rounce, D. R., King, O., McCarthy, M., Shean, D. E., & Salerno, F. (2018). Quantifying debris thickness of debris-covered glaciers in the Everest region of Nepal through inversion of a Subdebris melt model. *Journal of Geophysical Research: Earth Surface*, *123*(5), 1094–1115. https://doi.org/10.1029/2017JF004395

Rounce, D. R., & McKinney, D. C. (2014). Debris thickness of glaciers in the Everest area (Nepal Himalaya) derived from satellite imagery using a nonlinear energy balance model. *The Cryosphere*, *8*(4), 1317–1329. https://doi.org/10.5194/tc-8-1317-2014

Rounce, D. R., Quincey, D. J., & McKinney, D. C. (2015). Debris-covered glacier energy balance model for Imja–Lhotse Shar Glacier in the Everest region of Nepal. *The Cryosphere*, *9*(6), 2295–2310. https://doi.org/10.5194/tc-9-2295-2015

Rowan, A. V., Nicholson, L. I., Quincey, D. J., Gibson, M. J., Irvine-Fynn, T. D. L., Watson, C. S., et al. (2020). Seasonally stable temperature gradients through supraglacial debris in the Everest region of Nepal, Central Himalaya. *Journal of Glaciology*, *1–12*(261), 170–181. https://doi.org/10.1017/jog.2020.100

Scherler, D., Wulf, H., & Gorelick, N. (2018). Global assessment of supraglacial debris-cover extents. *Geophysical Research Letters*, *45*(21), 11798–11805. https://doi.org/10.1029/2018GL080158

Scherler, M., Schneider, S., Hoelzle, M., & Hauck, C. (2014). A two-sided approach to estimate heat transfer processes within the active layer of the Murtèl–Corvatsch rock glacier. *Earth Surface Dynamics*, *2*(1), 141–154. https://doi.org/10.5194/esurf-2-141-2014

Steiner, J. F., Litt, M., Stigter, E. E., Shea, J., Bierkens, M. F. P., & Immerzeel, W. W. (2018). The importance of turbulent fluxes in the surface energy balance of a debris-covered glacier in the Himalayas. *Frontiers of Earth Science*, *6*. https://doi.org/10.3389/feart.2018.00144

Sturm, M., & Benson, C. S. (1997). Vapor transport, grain growth and depth-hoar development in the subarctic snow. *Journal of Glaciology*, *43*(143), 42–59. https://doi.org/10.3189/S0022143000002793

Sturm, M., & Johnson, J. B. (1991). Natural convection in the subarctic snow cover. *Journal of Geophysical Research*, *96*(B7), 11657–11671. https://doi.org/10.1029/91JB00895

Thakuri, S., Salerno, F., Smiraglia, C., Bolch, T., D'Agata, C., Viviano, G., & Tartari, G. (2014). Tracing glacier changes since the 1960s on the south slope of Mt. Everest (central Southern Himalaya) using optical satellite imagery. *The Cryosphere*, *8*(4), 1297–1315. https://doi.org/10.5194/tc-8-1297-2014

van Woerkom, T., Steiner, J. F., Kraaijenbrink, P. D. A., Miles, E. S., & Immerzeel, W. W. (2019). Sediment supply from lateral moraines to a debris-covered glacier in the Himalaya. *Earth Surface Dynamics*, *7*(2), 411–427. https://doi.org/10.5194/esurf-7-411-2019

Wicky, J., & Hauck, C. (2020). Air convection in the active layer of rock glaciers. *Frontiers of Earth Science*, *8*. https://doi.org/10.3389/feart.2020.00335